Article:

Lawal, MS, Fairweather, M, Gubba, SR et al. (5 more authors) (2013) Large eddy simulations of wake-stabilised flares. Fuel Processing Technology, 112. 35 - 47. ISSN 0378-3820

https://doi.org/10.1016/j.fuproc.2013.02.018

Large Eddy Simulations of Wake-Stabilised Flares

M.S. Lawal[a], M. Fairweather[a], P. Gogolek[b], S.R. Gubba[a], D.B. Ingham[a], L. Ma[a,*],
M. Pourkashanian[a], A. Williams[a]

[a]*CFD Centre, Energy Technology and Innovation Initiative (ETII), University of Leeds, Leeds, LS2 9JT, UK*

[b]*CANMET Energy and Technology Centre Flare Test Facility, Natural Resources Canada, 1 Haanel Drive, Ottawa, Ontario K1A 1M1, Canada*

*Corresponding author, email: l.ma@leeds.ac.uk

ABSTRACT

This paper investigates the potential benefits, as well as limitations, of using the LES technique to predict the combustion efficiency, emissions and temperatures of wake-stabilised flares. LES calculations have been performed for two jet-to-cross-flow momentum flux ratios, with results compared with experimental data, where available, and with predictions of a RANS model closed using a second-moment turbulence closure. The flame fragmentation and the secondary flame zone attached to the release pipe at high jet-to-cross-flow momentum flux ratios, and their influence on the evolution of the counter-rotating vortex pair found in such flames, are discussed in detail, with realistic predictions being produced by the LES. The global mixing characteristics and the combustion efficiency of such flames are also compared with available data with reasonable agreement found. In all cases, LES predictions are found to be superior to equivalent RANS results, although the extra computational effort required in predicting species concentrations and flare efficiencies, in particular, may not be warranted.

Keywords: LES, flares, jet-in-cross-flow, counter-rotating vortices, pollutants.

1. Introduction

Flares are widely used in oil and gas industry for a controlled burning of gaseous hydrocarbons as a means of more environmentally friendly and cost effective disposal of waste gases. It is estimated that an average of approximately 150 billion m^3 of gas is flared annually worldwide. Despite of a significant amount of research and development on flaring technologies having been carried out, emissions from flares, in terms of both the radiation of heat and the release of pollutants, are still major concerns for the environment. This paper reports a new effort of using the Large Eddy Simulation (LES) technique to simulate the flames of wake-stabilised flares in order to investigate the potential benefits of using this technique to predict the combustion efficiency and emissions of industrial flares more accurately, which is critical to the flare system design and operation.

The flow field of a wake-stabilised flare is characterised by strong interactions involving the cross-flow, the fuel jet and the flare stack. The shear layer originating from these interactions generates organised vortices and their effects on the turbulent flow field are dominated by large-scale coherent structures [1, 2]. These large-scale structures have a significant influence on mixing within the flow, and the subsequent combustion characteristics and the emissions of the flare. In the flow regions dominated by such coherent structures, conventional turbulence models used in conjunction with Reynolds-averaged Navier-Stokes (RANS) solutions do not adequately resolve the turbulent mixing field [3]. As a result, RANS predictions of those combustion processes that are influenced by the coherent structures, such as the finite-rate kinetics involved in pollutant formation, are generally not in good agreement with experimental data. To provide a more accurate description of the coherent structure and their effect on turbulent mixing, flame structure and emissions, more sophisticated computational modelling approaches, such as large eddy simulations (LES), are required.

In LES, the large-scale, unsteady, three-dimensional turbulent eddies which contain most of the turbulence energy and control the dynamics of the flow field are resolved [4]. The small scale eddies are modelled through a sub-grid scale (SGS) model. Therefore, when compared to RANS, the LES approach offers the potential benefit of improving the description of the scalar mixing processes that are very important in chemical reactions [4]. Furthermore, LES inherently requires time dependent calculations which resolve multiple turbulent length scales, and hence this technique is capable of providing a more detailed description of the turbulent flow than the time-averaged flow field computed with RANS [4]. However, in turbulent flames, the molecular level mixing of those scalars that facilitate chemical reaction essentially occurs at small turbulence length scales that are usually significantly smaller than the LES grid size employed, and consequently, as in RANS, combustion needs to be modelled entirely in LES [4].

Some applications of LES to the study of non-reacting jets in cross-flow (JICF) can be found in the literature [5-7]. However, there are few published studies on the LES of jet flames in a cross-flow (JFICF), the configuration that approximates flares. This is because of the very high computational effort required for such calculations. Wang and Pitsch [8] did use the steady laminar flamelet and flamelet progress variable combustion models with LES to investigate the mixing and combustion process of a highly heated cross-flowing fuel jet in an industrial furnace. They found good agreement in the predictions of the major chemical species, such as CO_2 and O_2, with measured data. However, comparable agreement was not obtained for the trace species, CO and NO, particularly near the furnace wall. Smith [9] also used a massively parallel LES code (Arches) to study the impact of H_2S on the flare combustion efficiency. Although detailed reporting of this work is not as yet in the public domain, the preliminary results [9] show that an increase in the concentration of H_2S in the flare gas decreases both the carbon and sulfur conversion efficiencies.

Hence, the authors consider the investigation reported in this paper to be the first published application of LES to an industrial-scale, wake-stabilised flare configuration. In light of the substantial computational effort involved in LES-based calculations, the objective of the present investigation is to examine the potential benefits and limitations of the LES approach, over RANS simulations [10] employing a Reynolds stress turbulence model, in improving predictions of the complex flame structure that influences the flare combustion efficiency, temperature and emissions. The complex flow features of interest include the secondary flame region on the lee side of the flare stack, fragmentation of the flame by the cross-flow, the counter-rotating vortex pair and its influence on global mixing within the flow field.

2. Test Cases

The test cases considered are based on the experimental investigations performed at the flare test facility (FTF) at the CANMET Energy Technology Centre (CETC), Ottawa, Canada. The FTF consists of a once-through wind tunnel with a working section of length 8.2m and width 1.22m. The height of the tunnel is adjustable, starting from approximately 1.5m. A cylindrical flare release pipe, having a diameter of ≈ 5.25cm and length of ≈ 0.61m, is mounted at approximately 2.4m downstream of the cross-flow inlet plane. A schematic representation of the FTF is shown in Fig. 1, where the origin of the coordinate system is at the jet exit.

The test conditions examined consist of burning a jet of natural gas (95% CH_4, 2.4% C_2H_6, 0.06% C_3H_8, 1.74% N_2 and 0.81% CO_2) at two jet-to-cross-flow momentum flux ratios (R) of 0.256 and 0.005. The jet-to-cross-flow momentum flux ratio is defined as $R = (\rho u^2)_j/(\rho u^2)_{cf}$, where the subscripts j and cf denote jet and cross-flow, respectively. Most offshore solution gas flares burn natural gas fuels, hence its use to represent the waste gas in this study [2]. The corresponding Reynolds numbers based on the pipe diameter and cross-flow velocity are approximately 28,000 and 17,000, respectively. A summary of the flow conditions investigated is given in Table 1.

3. Numerical Models

LES based compressible flow simulation employing the Favre filtered equations for the conservation of mass, momentum and the mixture fraction, typically takes the following form, respectively:

$$\frac{\partial \bar{\rho}}{\partial t} + \frac{\partial \bar{\rho}\tilde{u}_i}{\partial x_i} = 0 \tag{1}$$

$$\frac{\partial \bar{\rho}\tilde{u}_i}{\partial t} + \frac{\partial \bar{\rho}\tilde{u}_i\tilde{u}_j}{\partial x_j} = -\frac{\partial \bar{p}}{\partial x_i} + \frac{\partial}{\partial x_j}\left(2\mu\tilde{S}_{ij} - \frac{2}{3}\mu\delta_{ij}\tilde{S}_{kk} - \tau_{ij}\right) + \bar{\rho}g_i \tag{2}$$

$$\frac{\partial \bar{\rho}\tilde{Z}}{\partial t} + \frac{\partial \bar{\rho}\tilde{u}_j\tilde{Z}}{\partial x_j} = -\frac{\partial}{\partial x_j}\bar{\rho}\left(\widetilde{u_j Z} - \tilde{u}_j\tilde{Z}\right) + \frac{\partial}{\partial x_j}\left(\frac{\mu_t}{\sigma_t}\frac{\partial \tilde{Z}}{\partial x_j}\right) \tag{3}$$

where ρ is the density, u_i is the component of the velocity in the i direction, Z is the mixture fraction, p is the pressure, g_i is the gravitational acceleration, τ_{ij} is the stress tensor, μ_t is the turbulent dynamic viscosity and σ_t is the turbulent Schmidt number, typically with a value of

0.85. An over-bar describes the application of the spatial filter, while the tilde denotes Favre filtered quantities. In order to close the set of Favre filtered governing equations, sub-grid scale models for turbulence and the scalar flux must be employed, as discussed in the following section.

3.1 Modelling of SGS momentum and scalar fluxes

The filtered Navier-Stokes equation yields an unknown sub-grid scale stress term, τ_{ij}, due to the decomposition of the non-linear convection terms, which must be closed either by using models or solving complex additional transport equations. This term is generally referred to as a residual stress and represents the impact of the unresolved velocity components on the resolved ones. Mathematically, and as noted, this term arises from the non-linearity of the convection term, which does not commute with the linear filtering operation. In the present work, this term is modelled by the widely used classical Smagorinsky turbulence model [11], based on the linear eddy viscosity as follows:

$$\tau_{ij} = 2\mu_t \tilde{S}_{ij} + \frac{1}{3}\tau_{kk}\delta_{ij} \tag{4}$$

where $\tilde{S}_{ij} = \frac{1}{2}\left(\frac{\partial \tilde{u}_i}{\partial x_j} + \frac{\partial \tilde{u}_j}{\partial x_i}\right)$. The turbulent dynamic viscosity μ_t is modelled as $\mu_t = (C_s\Delta)^2|\tilde{S}|$ in which C_s is the Smagorinsky model constant and Δ is the local grid scale. The dynamic Smagorinsky-Lilly model has been used to calculate the model constant, C_s, based on information provided by the resolved scales of motion [12]. This approach is effective in particular for flows containing localised regions of low Reynolds number, and in predicting the backscatter of energy from the sub-grid to the resolved scales. Therefore, the dynamic procedure is suited to the JFICF, in which some regions of the flow field are characterised by a low Reynolds number. In this work, the top-hat filter is applied and the filter-width is computed implicitly based on the finite-volume approach. The filter-width is defined as the cube-root of the grid cell volume ΔV, which represents the characteristic length scale. The unresolved scalar fluxes in Eq. (3) are described using the simple gradient assumption, with a dynamic determination of μ_t and σ_t [12]. The sub-grid scale turbulence flux, q_j, of a scalar, ϕ, is modelled as follows:

$$q_j = -\frac{\mu_t}{\sigma_t}\frac{\partial \phi}{\partial x_j} \tag{5}$$

3.2 Combustion and thermal radiation modelling

The thermo-chemistry of the combustion process is closed through the simplified laminar flamelet equation in mixture fraction space [13, 14], namely:

$$\bar{\rho}\frac{\partial \tilde{Y}_i}{\partial t} = \bar{\rho}\frac{\tilde{\chi}}{2}\frac{\partial^2 \tilde{Y}_i}{\partial Z^2} + \tilde{w}_i \tag{6}$$

$$\tilde{\rho}\frac{\partial T}{\partial t} = \bar{\rho}\frac{\tilde{\chi}}{2}\frac{\partial^2 \tilde{T}}{\partial Z^2} - \frac{1}{c_p}\sum_i \tilde{H}_i \tilde{w}_i + \bar{\rho}\frac{\tilde{\chi}}{2c_p}\left(\frac{\partial c_p}{\partial Z} + \sum_i c_{p,i}\frac{\partial \tilde{Y}_i}{\partial Z}\right)\frac{\partial T}{\partial Z} \tag{7}$$

where Y_i is the mass fraction of species i, χ is the scalar dissipation rate and w_i is the reaction rate of the i^{th} species. In Eq. (7), T, H, c_p, and $c_{p,i}$ are, respectively, the temperature, specific enthalpy, mixture-averaged specific heat and specific heat of species i. The flamelet model relates the chemical state of the mixture to the mixture fraction field with the conditional averaged scalar dissipation rate as the non-equilibrium parameter. The scalar dissipation rate is obtained from an algebraic model in the form:

$$\tilde{\chi} = 2(C_z\Delta)^2|\tilde{S}|\left|\frac{\partial \tilde{Z}}{\partial x_j}\right|^2 \tag{8}$$

where C_z is the model constant, which are computed dynamically. The detailed combustion chemistry is incorporated through the GRI-MECH 3.0 [15] chemical kinetic mechanism. The steady flamelet model (SFM), i.e. Eqs. (6) to (8), is solved (without the time dependent term) for 16 flamelets for values of χ ranging from 0.0001 to 39 s^{-1}. This range has been found to provide adequate accuracy in accounting for the relaxation effect associated with smaller values of χ on the thermal radiation and trace emission species [16]. The computed mixture fraction, its sub-grid variance and the scalar dissipation serve as input for computing the sub-grid probability density function (β-PDF) of the mixture fraction. Based on the PDF integration, the mean values of the thermo-chemical state of the mixture are computed and tabulated in the flamelet look-up table. This table is updated through linear interpolation during the calculation of the flow field.

Ideally, a transport equation for the sub-grid Favre variance of the mixture fraction, $\tilde{Z}''^2$, should be solved, and this requires detailed modelling of the filtered scalar dissipation rate. In the absence of a satisfactory model for the later, the local equilibrium model for the sub-grid variance of the mixture fraction is employed. This is represented as follows:

$$\tilde{Z}''^2 = C_v\Delta^2\left|\frac{\partial \tilde{Z}}{\partial x_j}\right|^2 \tag{9}$$

The model constant, C_v in Eq. (9), is also computed dynamically. In combustion modelling using LES, the SFM is often used because of its simplicity when implementing complex chemistry effects and its reasonable computational cost. Moreover, the flamelet paradigm can provide an accurate description of turbulent flames containing large scales and low turbulence intensities. Also, the model is valid for combustion chemistry that is mixing limited and where the reactions tend to occur near the mean stoichiometric region [17].

However, the SFM assumption has limitations under certain conditions, such as those involving local extinction and re-ignition, radiative heat transfer, and the formation of pollutants species with long residence times [18]. These limitations are associated with the inability of the SFM to resolve the fluctuations in the scalar dissipation rate [19]. In the present investigation, these fluctuations are partly taken care of through the unsteady calculation of the flow field. Successful applications of the SFM model in LES computations of practical flames include [8, 20, 21].

In the RANS calculations, similar approaches are employed as in the LES for combustion simulation, except that the full spectrum of the turbulence scales is modelled using a Reynolds stress turbulence model. The radiative heat transfer in the flame is modelled using the discrete ordinate method [22] for both the LES and RANS calculations. The three gray gas based weighted-sum-of-gray-gases approach is used in calculating the absorption coefficient for the main participating species in methane-air flames, namely, CO_2 and H_2O [23].

The implementation of the flamelet and the radiation models employed in the paper are detailed in the ANSYS FLUENT [23]. Further, the natural gas used in the test cases contains

95% methane which is not expected to produce much soot under the condition investigated. Therefore soot formation and its influence on the radiative heat transfer are not included in the simulations reported in this paper.

4. Numerical Grid, Boundary Conditions and Calculation Procedure

The experimental test facility described in Section 2 was represented by a three-dimensional, non-uniform mesh in the Cartesian co-ordinate system that spanned 23*d* in the spanwise, 157*d* in the streamwise and 28*d* in the vertical directions, where *d* is the outer diameter of the release pipe. The location of the pipe was at a distance of 46*d* from the cross-flow inflow plane and the jet exit extended up to 11*d* into the domain. The computational domain was discretised by employing a structured, hexahedral mesh. For the RANS calculations, the mesh employed consisted of 295 × 145 × 51 (2.2 million) grid points in the x, y and z directions, respectively. This mesh distribution was refined to 350 × 180 × 75 (4.7 million) grid points for the LES calculations. The appropriateness of this grid resolution for the LES simulations is discussed in Section 4.3.

4.1 Boundary conditions

LES requires appropriate initial and unsteady inlet boundary conditions which exert an influence on the development of the downstream flow. To this end, the solution from the steady RANS calculation obtained using the Reynolds stress turbulence model (RSM) was used as the initial condition in the LES calculations. To generate the required unsteady perturbation on the mean velocity profile, a modified two-dimensional vortex method [24] was employed at the cross-flow and the pipe inlets, where Dirichlet boundary conditions were specified. The turbulence intensities at these inlets were 1% and 5%, respectively, which is within the ranges reported in similar experiments [2]. To account for the non-uniformity of the jet flow exiting the flare release pipe, the flow within the pipe was solved for numerically. This allows for the natural evolution of the turbulent jet flow as it emerges into the cross-flow. The outlet of the domain was set to be a Neumann boundary with a zero gradient condition prescribed for all the flow variables, except pressure. Near the solid boundaries, the wall model was adopted where the velocity at the solid wall is adjusted so that the local shear flow is enforced to satisfy the logarithmic law of the wall [25]. This model was used at the solid boundaries, corresponding to the top, bottom and side walls of the tunnel.

4.2 Calculation procedure

All the filtered transport equations are solved, with the time dependent terms, using the numerical methods embodied in the ANSYS FLUENT 12.1 CFD code. The governing equations are advanced in time using a second-order semi-implicit scheme. The momentum and energy equations are discretised using the bounded-central differencing scheme, which is second-order accurate. To reduce the effect of numerical diffusion on the smallest resolved scales and their energy content, the third-order MUSCL scheme is used for the scalar transport equations. The SIMPLE algorithm [26] is employed for the pressure-velocity coupling. The calculations are performed for several fluid flow times that are required for the solution to reach a statistically steady state.

LES requires a substantially finer computational mesh when compared to RANS, and transient calculations with a sufficiently small time step carried out for a long enough period of time in order to obtain stable and accurate flow statistics. As a result, the computational cost of LES is typically orders of magnitude greater than that of a steady RANS calculation. In the studies reported in this paper, a typical steady state RANS calculation took approximately 100 hours on a four processor computer, whilst the LES took at least 1,400 hours on the University of Leeds' high performance computer cluster using 8-processors.

4.3 Turbulence kinetic energy resolution

Although there is no universally accepted measure for a required LES grid resolution, it is imperative to assess the quality of the grid employed before presenting results. In order to assess this, a turbulence resolution parameter, *M*, defined as the fraction of the turbulence kinetic energy being modelled by SGS, is estimated by following the criterion explained in [27], namely:

$$M \equiv \frac{k_{sgs}}{k_{sgs} + k_{res}} \tag{10}$$

where k_{sgs} is the SGS turbulence kinetic energy and k_{res} is the resolved turbulence kinetic energy, which is defined as [27]:

$$k_{res} \equiv \frac{1}{2}\left\langle \left(\tilde{u}_i - \langle \tilde{u}_i \rangle\right)\left(\tilde{u}_i - \langle \tilde{u}_i \rangle\right) \right\rangle \tag{11}$$

where $\tilde{u}_i$ and $\langle \tilde{u}_i \rangle$ are the filtered and mean velocity components, respectively. Eq. (10) requires the determination of k_{sgs}, which is estimated using the expression given in [28], namely:

$$k_{sgs} = \frac{1}{(C_{v1}\Delta)^2}\mu_t^2 \qquad (12)$$

where C_{v1} is a constant set to be 0.1 and Δ is the local grid scale. The criterion *M* defined in Eq. (10) varies between 0 (equivalent to DNS) and 1 (equivalent to RANS). Therefore, a smaller value of *M* indicates that a greater proportion of the turbulence kinetic energy is resolved in the calculations and typically a value of $M < 0.2$ very where in the solution domain is desired.

Fig. 2 shows an example of the spatial distribution of *M* on the mid-plane of the computational domain obtained from the time-averaged LES solution of the flow field for Case 1 ($R = 0.256$). It is clear from the figure that a significant portion of the domain is covered by regions with $M \leq 0.2$. This corresponds to regions where approximately 80% of the turbulence kinetic energy is resolved. For high Reynolds number flows, Celik et al. [29] considered that resolving 70 to 85% (M <0.3) of the turbulence kinetic energy is sufficient. From Fig. 2, it is evident that the grid resolution employed is sufficiently fine to resolve the bulk of the turbulence kinetic energy remote from the walls of the release pipe. Only in a small region immediately behind the release pipe is the *M* greater than 0.2 and we believe that this is acceptable.

5. Results and Discussion

In this section, the results obtained from the LES and RANS calculations are presented and discussed. Starting with a description of the flame appearance, the instantaneous and mean temperature fields are compared with the experimental data from similar flare experiments

[2]. Subsequently, the mean profiles of the velocity, the Reynolds stresses and turbulence intensity are presented. Furthermore, the mean and root-mean-square (RMS) temperature profiles and the volume fraction of the important pollutant species, CO_2, CO, and NO_x, as well as the combustion efficiency of the flame are reported. To illustrate the relative benefit of the LES approach in comparison with the most sophisticated RANS turbulence model, the Reynolds stress model, a comparison of the results obtained from the two techniques is made.

In order to compare the results obtained from the LES calculations with the experimental data, temporal averages of the instantaneous simulation results must be taken at specific sampling time intervals. The flow time and sampling intervals chosen must also be sufficient to ensure the temporal average statistics have converged. To determine whether the LES calculations have reached a statistically steady state, the profiles of the mean mixture fraction were taken after 0.725s at three successive intervals of 0.05s for Case 1 at a location x/d = 2.0, as presented in Fig. 3. Clearly, the mixture fractions obtained at the three sampling intervals are similar, indicating that the flow field solution is statistically steady. Therefore, the LES results reported in this section are for a flow time of 1.30 s after which the LES was terminated for computational expedience.

5.1 Flame appearance and flow features

The appearance of the flame is discussed in terms of the instantaneous and mean temperature fields. Fig. 4 shows plots of the predicted instantaneous and mean temperature contours, on the central plane of the flow, from both the LES and RANS simulations for Case 1. The instantaneous temperature contour from the LES, shown in Fig. 4(a), reveals that the flame is stabilised in the wake of the release pipe and that it is fragmented due to the unsteady fluctuations caused by the high velocity cross-flow. These fragmentations create an interspersed region of unburned fuel (the low temperature region in the figure) surrounded by the discrete pockets of the burning diffusion flame. The flame regions are composed of organised unsteady vortices that are comparable to the experimental short-time exposure photographs of a similar flare flame shown in Fig. 5(a) [2]. Also evident in the LES predictions of the mean temperature contours, shown in Fig. 4(b), are the coherent eddies visible at a lower scale. It is noted that the experiment reported in [2] is slightly different from the case simulated in this paper. It did demonstrate the presence of typical unsteady fluctuations and fragmentation of the flame from flares which are not resolved by the RANS solution, as shown in Fig. 4(c). This is an indication of the limitations of the RANS approach in resolving unsteady coherent flow structures existing in flames in cross-flow.

Furthermore, the time-averaged LES solution for the mean temperature contours shown in Fig. 4(b) provides a good prediction of the visual shape and position of the flame, and it is comparable to the long-exposure photographic image from similar flare experimental data presented in Fig. 5(b) [2]. It should be noted that, although the RANS approach predicted a narrower flame brush, it still resolved the gross features of the flame. Further, the LES prediction of a peak mean temperature of 1900 K agrees well with the value of 1860 K reported in an experimental investigation of a lifted natural gas flame in a cross-flow [30]. However, the RANS approach significantly under-predicts the peak mean temperature by about 110 K. Thus, it may be inferred that the improved resolution of the large-scale turbulence motion in the LES has the effect of improving the prediction of the physics and the thermo-chemistry of the flame.

Among the complex features in wake-stabilised flares is the presence of a secondary flame region attached to the leeside of the fuel release pipe, and the increase in the size of this region as the jet-to-cross-flow momentum flux ratio R decreases [31, 32]. At $R = 0.256$, Fig. 4(b) shows that this feature is adequately resolved by the LES. However, the RANS calculation, at the same value of R, did not resolve this feature, as is evident in Fig. 4(c). Fig.s 6(a) and (b) present the predicted flame temperatures obtained using LES and RANS, respectively, at a lower jet-to-cross-flow momentum flux ratio, i.e. $R = 0.005$ (Case 2). Here, the RANS calculation, just as for the LES (Fig. 6(a)), is able to resolve this secondary flame region attached to the fuel pipe, as shown in Fig. 6(b). Therefore, it is clear that RANS is only able to resolve the secondary flame region in wake-stabilised flares at very low values of R [10], whilst the LES is capable of resolving this complex flow feature at both low and high values of R. It is very important to predict this secondary flame region correctly because it is where low combustion efficiency occurs producing significant quantity of emissions of unburned hydrocarbons (UHCs), as will be discussed further later.

5.2 Flow field statistics

An assessment of the flow field statistics, such as the resolved mean velocity, Reynolds stresses and turbulence intensity, are important in validating the results obtained from the numerical computations. In the absence of experimental data for these flow variables for the flare configuration investigated, a qualitative comparison of the predictions has been made, where possible, with the experimental data obtained for a propane wake-stabilised JFICF that has a similar jet-to-cross-flow momentum flux ratio to one of the cases investigated in this paper [32]. Although natural gas flames are less luminous and shorter than propane flames, it has been reported that the flow structures in both flames are essentially the same at similar values of *R* [2]. Therefore, the flow field statistics of the natural gas flame investigated in this paper are expected to be similar to those obtained in the propane flame, at similar values of *R*. Since many of the interesting features of the flow occur on and off the central plane, the flow field statistics reported in the following sections are for the symmetry plane itself, and for a spanwise plane that is perpendicular to the streamwise direction.

5.2.1 Velocity statistics

Fig. 7 (a-f) presents the spanwise velocity profiles from the LES and RANS predictions for Case 1 near to the bend of the jet flame ($x/d = 2$) at three different vertical distances from the jet exit, i.e. $y/d = 2.0$, 0.0 and -1.4. The cross-flow and jet velocity profiles are represented by U (x-component of the mean velocity) and V (y-component of the mean velocity), respectively. Above the jet exit ($y/d = 2$), both the LES and RANS predict an increase in the U velocity profile as the cross-flow encounters the jet, Fig. 7(a). The spanwise location of the peak U velocity is slightly off the symmetry plane, and this is consistent with experimental data [32]. Compared to the 19% increase in the U velocity observed in the experimental data, the LES simulation predicted a 10% increase, while the RANS showed only a 1% increase. It is evident that while the LES somewhat under-predicts the increase, the RANS considerably under-predicts it. At the same downstream location ($x/d = 2$), the V velocity profiles show a peak on the symmetry plane, and away from this plane the value of the V velocity decreases monotonically, see Fig. 7(b). Interestingly, at this location, both the LES and RANS predicted similar trends for the V velocity, which are in good agreement with the experimental data [32].

In the vicinity of the jet exit ($y/d = 0$), Fig. 7(c) shows that the LES predicted U velocity profile dips on the plane of symmetry and peaks at about $z/d = 1.0$. This is a characteristic of wake flow initiation and is in excellent qualitative agreement with the experimental data. Although the RANS predicted a similar trend, the location of the minimum is off the symmetry plane. This discrepancy may be due to the inability of the RANS technique to resolve the coherent motion of the fluid in this region. On the other hand, the LES prediction of the V velocity profile shows double dips and peaks, as in Fig. 7(d). The initial minima is on the symmetry plane, whereas the second and lower minima occurs off this plane, at $z/d = 1.0$. This sudden decrease in the axial velocity is an indication of vortex breakdown. This trend is consistent with the presence of a recirculation bubble that has been reported in experimental measurements [32]. In contrast, the RANS predictions show a single peak whose location coincides with the second dip in the LES results. The peak of the V velocity profile is an indication of the up-streaming of the shear layer in the vicinity of the jet exit. Clearly, the LES is able to resolve this up-streaming reasonably well in comparison to the experimental data.

Below the jet exit ($y/d = -1.4$), the U velocity profile dips on the plane of symmetry, whereas the trend in the V velocity differs between the two prediction methods, as shown in Figs. 7(e) to (f). In this low pressure wake region, V shows negative values due to the reverse flow that creates a compressive stress on the pipe wall. It is observed that the LES simulation resolves more of this reverse flow as indicated by its prediction of much lower negative values for the V velocity, as compared to the RANS solution. The reverse flow occurring in this region is responsible for the creation of a low pressure zone where some of the fuel that is stripped from the pipe flow by the cross-flow is drawn into. Since the LES provides better predictions of this phenomenon, it explains why this technique is able to resolve the secondary flame region attached to the release pipe more accurately, as discussed in the previous section.

5.2.2 Reynolds shear stress

In the flows studied, the magnitude of the subgrid-scale shear stresses is quite low and does not significantly contribute to the total Reynolds stresses. Consequently, only the resolved components of the Reynolds shear stresses are reported in this section. Fig. 8 shows the profiles of the resolved x-y component of the Reynolds stress, $\tau_{xy} = \rho \overline{u'v'}$, for Case 1 taken at two vertical locations, *y/d* = 0 and *y/d* = -1.4, corresponding to the region in the wake of the jet and the wake of the release pipe, respectively, at *x/d* = 2. In the wake of the jet at *y/d* = 0, see Fig. 8(a), the Reynolds shear stress predicted by the LES peaks at *z/d* = 0.6 and has a dip on the plane of symmetry. This trend is consistent with previous experimental observations [32]. The location of the maximum Reynolds stress corresponds to the shear-layer where there is significant fuel-air mixing. In comparison to the RANS, the LES predicts a significantly higher peak value for the stress in the bend of the jet where the presence of coherent turbulent structures has been reported [32]. Therefore, the under-prediction of the magnitude of the Reynolds shear stress by the RANS can be attributed to the fact that it does not account for the effect of the coherent structures in this region. However, in the free stream, where these coherent structures are less significant, both calculations predict a similar level of the shear stress.

Below the jet exit, in the wake of the pipe at *y/d* = -1.4, see Fig. 8(b), the Reynolds stress behaves similarly to the trends discussed above, but there is less discrepancy between the LES and the RANS predictions. An examination of the Reynolds stress in the wake of the pipe and in the wake of the jet shows that the former is much lower than the latter, as can be seen by comparing Figs. 8(a) and (b). This trend may be attributed to the strong shear effect in the wake of the jet and the associated velocity fluctuations generated by the shear-layer, which are better resolved by the LES.

5.2.3 Turbulence intensity

The distributions of the turbulence intensity in the wakes of the jet and the pipe at $x/d = 2$ for Case 1 are presented in Fig. 9. The trend in the turbulence intensity is similar to that in the Reynolds shear stress discussed in the previous section. However, in this case, the agreement between the LES and RANS predictions is much better. In Fig. 9(a), the peak turbulence intensity in the cross-flow near the jet exit is approximately 2.3%, which is approximately twice the value prescribed at the cross-flow inlet, and half that at the jet inlet. As expected, this is an indication that turbulence is generated in the shear layer near the jet exit. Similar to the shear stress, the LES predicts a slightly higher turbulence intensity in comparison with the RANS. On the other hand, for the turbulence intensity in the wake of the pipe, see Fig. 8(b), the agreement between the LES and the RANS predictions is quite good. This suggests that, as in the LES, the spanwise distribution of the turbulence intensity in this region is adequately resolved by the RANS. It should be noted that the turbulence intensity in the wake of the pipe is considerably lower than it is in the wake of the jet. This is likely due to the flow reversal and stagnation in the wake of the pipe, resulting in the lower turbulence intensity.

The vertical distribution of the turbulence intensity at two locations downstream of the jet exit is presented in Fig. 10. Fig. 10(a) shows that the peak turbulence intensity in the near-field ($x/d = 2$) is approximately twice the intensity in the far-field, see Fig. 10(b). This trend agrees with earlier experimental findings [32]. The far-field is the region where the magnitude of the counter-rotating vortex pair increases (as discussed in section 5.3 below). Therefore, it is likely that the vortex roll-up associated with the counter rotation causes a loss of vorticity in the mean flow, and thus results in a reduction in the turbulence intensity. The LES predicts a greater peak intensity near the jet exit, in comparison with the peak value obtained when employing the RANS. However, further downstream, the RANS predicts a greater peak intensity relative to the LES. Overall, it is evident from the results presented that due to high shear stresses and turbulence intensities in the wake of the jet, which correspond to the shear layer, the RANS predictions of the turbulence intensity are lower than those obtained when using the LES. This is an indication that the LES resolves more of the turbulent activity in the flow field.

However, in the wake of the pipe, where there are lower values of both the shear stress and turbulence intensity, the agreement between the two calculation approaches is better. The over-prediction and under-prediction, respectively, of the peak Reynolds shear stress and turbulence intensity by the RANS is likely to be a consequence of its inability to account for the coherent turbulent structures' contribution to the overall mixing in the flow field. This can be attributed to the limitations of the RANS approach in resolving such coherent structures [3] in the flow field.

5.3 Counter rotating vortex pair

The interaction between the jet and the cross-flow produces a number of secondary coherent flow structures. In wake-stabilised flares, the two main coherent structures are one on the upper bend of the jet surface near the jet exit, which originates in the shear layer and contributes to the significant mixing in the near-field, as has been discussed in the preceding sections, and the counter rotating vortex pair (CVP) downstream of the jet exit. The CVP has been shown to have a strong influence on the flame behaviour and on the overall mixing in the far-field. In addition to using vorticity and pressure distributions to identify coherent structures such as the CVP [6], the mean temperature distribution can also be employed to quantify their influence on scalar fields within these flows.

To visualise the influence of the CVP, the predicted half-plane temperature contours on various *y-z* planes obtained from LES and RANS calculations are presented in Figs. 11 and 12 for Cases 1 and 2, respectively. These temperature contours are for five equal spaced streamwise locations, from $x/d = 5$ to 25. For Case 1 ($R = 0.256$), it is evident from Fig. 11 that on the plane at $x/d = 5$, which corresponds to the location nearest the jet exit, the size of the CVP is small and its centre is slightly below the jet exit plane. With an increase in the streamwise distance, the CVP changes position and strength, and its effect on the shape of the scalar field becomes fully developed (more kidney-like) in the far-field, which occurs at $\approx x/d = 25$. This is believed to correspond to the location where the jet flame becomes approximately self-similar. The increase in the magnitude of the CVP with downstream distance is an indication of a general increase in the size of the bent-over flame itself. This predicted trend is similar to previous experimental observations in both non-reacting and reacting JFICF at higher values of *R* [33, 34]. Interestingly, both the LES and RANS predictions of the evolution of the CVP and its influence on the temperature field are qualitatively similar.

For the flow condition at $R = 0.256$, it is evident that the CVP becomes fully developed, as show in Fig. 11(a) and (b). This is contrary to the conclusion of other authors, that in wake-stabilised flares at values of $R < 1.0$ the CVP does not become fully developed [32]. To investigate this aspect further, the temperature contours for the flow condition at a significantly lower value of R (i.e. 0.005, Case 2) are shown in Fig. 12(a) and (b). Noticeably, there is a considerable reduction in the size of the CVP at $R = 0.005$ in comparison to $R = 0.256$. Nevertheless, the CVP does become fully developed at $R = 0.005$, as indicated by its influence on the temperature field and the latter's kidney-like shape, although compared to the higher R case this is at a much smaller scale. This suggests that the CVP, being a dominant feature of the JFICF, can still fully develop even at low values of the jet-to-cross-flow momentum flux ratio, but its size is significantly dependant on latter.

An explanation of the differences in the CVP development between the two flow conditions is that, at $R = 0.256$, the CVP develops more gradually, and hence persists over much longer downstream distances. In contrast, at $R = 0.005$, the CVP develops much more quickly and persists over a relatively short downstream distance. Consequently, it can be observed that the temperature is considerably higher within the first two planes, at $x/d = 5$ to 10, for the flow condition at $R = 0.005$, see Figs. 11 and 12. This matches closely with the region of intense mixing, corresponding to where the Reynolds stresses and turbulence intensity have peak values. This observation is in accord with experimental findings in the non-reacting JICF, where it has been shown that the largest mixing improvement due to a reduction in R occurs in the near-field region [35]. However, for the flow condition at $R = 0.256$, at corresponding locations, both the temperature and the size of the CVP are still evolving. Hence, peak temperature values in this case occur further downstream. This suggests that the gradual development of the CVP at higher values of R allows vorticity and mixing in the flow field to be sustained over greater downstream distances, which enhances overall mixing and the combustion efficiency of the flame. This finding is consistent with experimental observations in which the poor efficiency of flares at very low values of *R* has been reported [2].

A qualitative comparison of the contour plots in Figs. 11 and 12 also shows that the maximum size of the CVP predicted by the LES is slightly larger than that obtained from the RANS. This suggests that the LES prediction of the global mixing strength in the flow field is correspondingly greater, since the CVP does enhance turbulent mixing in the far-field. It has been shown that in flows containing large spanwise-orientated coherent turbulent structures, such as the CVP, Reynolds-averaging over-predicts entrainment in moving fluids [3]. This affects the prediction of both mixing and chemical reaction, as well as the size of the recirculation zone, as is particularly evident in Fig. 11(b).

5.4 Temperature profiles

Mean radial temperature profiles for Case 1 at two downstream distances are presented in Fig. 13. In the near-field of the flame, Fig. 13(a) at x/d = 5.7, the expected bell shaped temperature profile and its double peaks are resolved by both the LES and RANS approaches. The double peak suggests a diffusion-controlled combustion process due to the fuel-air interface reaction near the jet exit. These predictions are in good qualitative agreement with the experimental temperature profiles in a natural gas flame in a cross-wind reported in [30]. The LES prediction of the peak mean temperature near the jet exit (x/d = 5.7) is approximately 100 K lower than the predicted RANS value. In addition, in the LES prediction, the peak temperature is located below the jet exit (at y/d = -2.0), in the region corresponding to the planar recirculation zone where there is less cross-flowing air to cool the flame. This is consistent with the experimental observation made for a propane-air JFICF at a similar value of R [31]. However, in the case of the RANS results, the two peak temperatures, as well as most of the flame zone, are above the jet exit plane. This is an indication that, in comparison to the LES, the RANS predicts a greater vertical rise of the flame. Despite this discrepancy, in the near-field region, both the LES and RANS predict essentially similar temperature profiles.

In the far-field region, at $x/d = 22$, both the LES and RANS predict a single peak in the mean temperature profiles, as shown in Fig. 13(b). Relative to the peak temperature in the near-field, in the far-field this temperature is approximately 130K higher. A similar magnitude of temperature difference is also observed between the RANS and the LES, with the latter having the lower value.

The resolved RMS temperature profiles obtained from the LES and RANS approaches at the same two downstream locations for Case 1 are shown in Fig. 14. In the near-field, Fig. 14(a), the two calculations predict a similar peak RMS temperature, with these profiles exhibiting larger variability than do the mean temperature profiles. In addition to contributing to the mixing, these fluctuations also cause fragmentation of the flame, as shown in Fig. 4(a), which is better resolved in the LES than in the RANS predictions. In contrast, in the far-field, the LES predicts a much higher RMS temperature than the RANS. Since chemical reactions progress at the smallest scales of turbulence, combustion is a SGS phenomenon. Therefore, the finer grid resolution used in the LES is able to better resolve the flame wrinkling and fluctuations, as shown earlier in Figs. 4(a) and (b), and this is likely responsible for the higher RMS temperature predicted by the LES in the far-field.

5.5 Chemical species and combustion efficiency

A major challenge in the mathematical prediction of industrial-scale flares has been the inability of numerical models to accurately estimate the concentrations of product species, and hence the flare combustion efficiency. In order to examine the predictions of species concentrations and the efficiency computed with the LES and RANS approaches, a quantitative comparison of the volume fractions of some of the important species, and the combustion efficiency, with the FTF experimental data is presented in Table 2 for Case 1 ($R = 0.256$). The uncertainties in the measurements of the species concentrations and the combustion efficiency were estimated to be less than 1% and 0.6%, respectively [2]. The combustion (or carbon conversion) efficiency is computed by mass as follows [2]:

$$\eta = \frac{CO_2}{CO_2 + CO + CH_4} \tag{13}$$

Since the combustion inefficiency, defined as 1-η, provides a clearer indication of the relative performance of the flaring processes, this quantity is also calculated and presented in Table 2. It should be noted that the emissions of CO and CH_4 are shown with their original measured data in vol% which may be converted into g/kg-fuel, and in this case they correspond to approximately 0.42 and 0.48 g/kg-fuel, respectively. It can be seen that the predictions of the major species O_2 and CO_2 are in good agreement with the experimental data, with the RANS slightly under-predicting the O_2 and CO_2 concentrations, and the LES slightly over-predicting them.

However, the figures associated with the unburned hydrocarbons (UHCs), composed mainly of methane, show greater discrepancies. Whilst the LES over-predicts the concentration of

CH_4 by less than 15%, the RANS significantly under-predicts it by about 50%. This gross under-prediction by the RANS is as expected, in view of the inability of this approach to accurately resolve the secondary flame attached to the release pipe (for the flow condition at $R = 0.256$, as discussed before). This region corresponds to where the presence of significant quantities of UHCs has been reported in both lifted and non-lifted flares [2, 36].

Both the LES and the RANS under-predict the CO species concentration. The formation of CO mainly results from the incomplete combustion of the hydrocarbon. Therefore, the under-prediction of CO by the RANS is consistent with the under-prediction of the UHCs, as discussed in the preceding paragraph. In contrast, the LES prediction is in better agreement with the data for this species. These results suggest that the higher experimental CO concentration may be due to the formation of coherent structures. In a previous study [37], it has been shown that the final CO and CH_4 concentrations in these flames are determined by the composition of local pockets of gas, the presence of which is influenced by the coherent structures in the flow field [3].

The significance of all these species predictions on the computed efficiency of the flame can be observed in Table 2. In comparison with the LES, the significant under-prediction of the CO and CH_4 species by the RANS results in a slightly greater over-prediction of the experimental flare efficiency, with the combustion efficiencies and inefficiencies predicted by LES being in closer agreement with the experimental data. Ideally, in addition to the overall emissions, spatial distributions of CO and CH_4 concentrations, or heat release rate, are good indicators of reaction zones and reaction efficiency. Unfortunately, no measurement data are available for comparison with the computed results for the case studied.

Contrary to initial expectations of a significant improvement in the species concentrations predicted using the LES compared to the RANS solutions, the results presented in Table 2 show that the former is not significantly better than the latter. The reason for this is likely that molecular mixing of scalars, and hence chemical reactions, in turbulent flames occurs at the smallest turbulence scales. The reaction rate controlling processes at these scales are not resolved in LES; instead, they are modelled (as in RANS) through the SGS model [19, 27]. LES predictions of molecular mixing, chemical reactions and product species concentrations still have a first-order dependence on the SGS models employed [27]. Consequently, for the flow conditions investigated, the LES prediction of the species concentrations and flare combustion efficiency, though in closer agreement with the experimental data, does not show a remarkable improvement commensurate with the substantial extra computational effort required. It should note that for large scale industrial flares with relatively low combustion efficiency, the intermittency of the flame may play a more significant role in the formation of emissions, and therefore the difference between RANS and LES predictions may be more pronounced. However, with the substantial increase in the value of the Reynolds number of industrial flares the computational cost of employing LES may be prohibitive.

6. Conclusions

LES simulations of wake-stabilised flares have been performed, with the thermo-chemistry described using the laminar flamelet model. Results from the LES have been compared with experimental data as well as with solutions obtained using a RANS approach coupled to a Reynolds stress turbulence model. The LES predictions of the instantaneous and mean temperature contours within the flames are comparable to experimental short- and long-time exposure photographs of similar flares. This demonstrates that LES can potentially better capture the visual appearance of these flames, including their fragmentation and unsteady fluctuations. Whilst the LES predicted temperature contours resolve the secondary flame region attached to the flare fuel release pipe at a wider region of flow conditions, the RANS is only capable of predicting these complex features at very low values of the jet-to-cross-flow momentum flux ratio. The improved resolution of the large-scale turbulence structures and fluctuations by the LES therefore has the effect of improving the prediction of the physics and thermo-chemistry of the flame, in particular the significant amount of unburned hydrocarbons that may be produced in the secondary flame region.

A qualitative comparison of the predicted mean velocities, Reynolds shear stresses and turbulence intensities with experimental data has been presented. Due to the high shear stresses and turbulence intensities in the wake of the jet, the RANS predictions of these quantities are lower than those obtained in the LES. However, in the wake of the release pipe, where the magnitude of both the shear stresses and turbulence intensities is smaller, there is better agreement between the LES and RANS predictions. The over- and/or under-prediction of the peak Reynolds shear stresses and turbulence intensities observed in the RANS results is likely to be a consequence of this technique not adequately accounting for the contribution of coherent structures to the overall mixing in the flow field [3].

In terms of the mean and root mean square temperature fluctuation profiles predicted by the LES, the peak temperatures are located below the jet exit in the region corresponding to the planar recirculation zone. This is consistent with experimental data. Although the RANS predicts similar temperature contours, the peak flame temperature zone is located above the jet exit plane. Also, predicted species concentrations and the efficiency of such flames have been compared with experimental data. Although the LES predictions were in closer agreement with data than the RANS, they did not show a significant improvement in accuracy that was commensurate with the substantial extra computational effort involved.

Acknowledgments

M.S. Lawal acknowledges the financial support of the Nigerian Government provided through the Petroleum Technology Development Fund’s Overseas Scholarship Scheme (PTDF-OSS).

References

[1] R. F. Huang, J. M. Chang, Coherent structures in a combusting jet in crossflow, AIAA 32(6) (1994) 1120-1125.

[2] L. W. Kostiuk, M. R. Johnson, G. Thomas, University of Alberta Flare Research Project Final Report, University of Alberta, Alberta, 2004. http://www.mece.ualberta.ca/groups/combustion/flare/papers/Final%20Report2004.pdf

[3] C. M. Coats, Coherent structures in combustion, Progress in Energy and Combustion Science 22(1996) 427-509.

[4] H. Pitsch, Large-eddy simulation of turbulent combust ion, Annual Review of Fluid Mechanics 38(1) (2006) 453-482.

[5] L. L. Yuan, R. L. Street, Trajectory and entrainment of a round jet in crossflow, Physics of Fluids 10(9) (1998) 2323-2335.

[6] L. L. Yuan, R. L. Street, J. H. Ferziger, Large-eddy simulations of a round jet in crossflow, J. Fluid Mech. 379 (1999) 71-104.

[7] B. Wegner, Y. Huai, A. Sadiki, Comparative study of turbulent mixing in jet in cross-flow configurations using LES, International Journal of Heat and Fluid Flow 25(5) (2004) 767-775.

[8] L. Wang, H. Pitsch, Large-eddy simulation of an industrial furnace with a cross-flow-jet combustion system, Centre for Turbulence Research, Annual Research Briefs (2007) 231-240.

[9] P. Smith, Sour Gas Flare Simulations, Flare Simulations, Utah, USA, Institute for clean and secure energy, The University of Utah, 2008-2009. http://www.flaresimulations.org/arc/

[10] M. S. Lawal, M. Fairweather, P. Gogolek, D. B. Ingham, L. Ma, M. Pourkashanian, A. Williams, Predicting the flow structures of wake-stabilised jet flames in cross-flow, Combustion Science and Technology (under review).

[11] J. Smagorinsky, General circulation experiments with the primitive equations: I. The basic equations. Monthly Weather Review 91 (1963) 99-164.

[12] M. Germano, U. Piomelli, P. Moin, W. H. Cabot, A dynamic subgrid-scale eddy viscosity model, Phys. Fluids A 3 (7) (1991) 1760-1765.

[13] N. Peters, Laminar diffusion flamelet models in non-premixed turbulent combustion, Progress in Energy and Combustion Science 10(3) (1984) 319-339.

[14] N. Peters, Laminar flamelet concepts in turbulent combustion, Symposium (International) on Combustion 21(1) (1988) 1231-1250.

[15] G. P. Smith, D. M. Golden, M. Frenklach ,N. W. Moriarty, B. Eiteneer, M. Goldenberg, C. T. Bowman, R. K. Hanson, S. Song, W. C. Gardiner, V. V. Lissianski, Z. Qin, GRI-MECH 3.0, http://www.me.berkeley.edu/gri_mech/.

[16] M. S. Lawal, M. Fairweather, D. B. Ingham, L. Ma, M. Pourkashanian, A. Williams, A numerical study of emission characteristics of a jet flame in cross-flow, Combustion Science and Technology 182 (10) (2010) 1491-1510.

[17] R. W. Bilger, S. B. Pope, K. N. C. Bray, J. F. Driscoll, Paradigms in turbulent combustion research, Proceedings of the Combustion Institute 30(1) (2005) 21-42.

[18] H. Pitsch, M. Chen, N. Peters, Unsteady flamelet modeling of turbulent hydrogen-air diffusion flames, Symposium (International) on Combustion 27(1) (1998) 1057-1064.

[19] H. Pitsch, Improved pollutant predictions in large-eddy simulations of turbulent non-premixed combustion by considering scalar dissipation rate fluctuations, Proceedings of the Combustion Institute 29(2) (2002) 1971-1978.

[20] V. Raman, H. Pitsch, Large-eddy simulation of a bluff-bodystabilized non-premixed flame using a recursive filter-refinement procedure, Combustion and Flame 142(4) (2005) 329-347.

[21] Kempf, R. P. Lindstedt, J. Janicka, Large-eddy simulation of a bluff-body stabilized nonpremixed flame, Combustion and Flame 144(1-2) (2006) 170-189.

[22] E. H. Chui, G. D. Raithby, Computation of radiant heat transfer on a nonorthogonal mesh using the finitevolume method, Numer. Heat Tr., B-Fund. 23 (1993) 269-288.

[23] ANSYS FLUENT, Version 12, Ansys Inc. USA, 2009.

[24] F. Mathey, D. Cokljat, J. P. Bertogolio, E. Sergent, Specification of LES inlet boundary condition using vortex. method, Progress in Computational Fluid Dynamics, an International Journal 6(1-3) (2006) 58-67.

[25] H. Werner, H.Wengle, Large-eddy simulation of turbulent flow over and around a cube in a plate channel. 8th Symposium on Turb. Shear Flows, Munich, Germany, (1993), 155-168.

[26] S. V. Pantakar, Numerical Heat Transfer and Fluid Flow, McGraw Hill, New York, 1980.

[27] S. B. Pope, New Journal of Physics 6(35) (2004) 1-24.

[28] P. Sagaut,,Large Eddy Simulation for Incompressible Flows An Introduction, 2002, Germany, Springer

[29] Celik, Z. N. Cehreli, I.Yavuz, Index of Resolution Quality for Large Eddy Simulations, ASME, J. Fluids Engng. 127 (2005) 949-958.

[30] A.D. Birch, D. R. Brown, M. Fairweather, G. K. Hargrave, An experimental study of a turbulent natural gas jet in a cross-flow Combustion Science and Technology 66(4) (1989) 217-232.

[31] S. R. Gollahalli, B. Nanjundappa, Burner wake stabilized gas jet flames in cross-flow, Combustion Science and Technology 109(1) (1995) 327-346.

[32] R. F. Huang, S. M. Wang, Characteristic flow modes of wakestabilized jet flames in a transverse air stream, Combustion and Flame 117(1-2) (1999) 59-77.

[33] S.H. Smith, M.G. Mungal, Mixing, structure and scaling of the jet in crossflow, Cambridge Journals Online 357 (1998) 83-122.

[34] S. R. Gollahalli, T. A. Brzustowski, H. F. Sullivan, Characteristics of a turbulent propane diffusion flame in a crosswind, Trans Can Soc Mech Eng 3(1975) 205-214.

[35] T. F. Fric, Skewed shear-layer mixing within a duct, AIAA 34(4) (1995) 847-849.

[36] R.V. Bandaru, S. R. Turns, Turbulent jet flames in a crossflow: effects of some jet, crossflow, and pilot-flame parameters on emissions, Combustion and Flame 121(1-2) (2000) 137-151.

[37] H. K. Chagger, J. M. Jones, M. Pourkashanian, A. Williams, The nature of hydrocarbon emissions formed during the cooling of combustion products, Fuel 76(9) (1997) 861-864.

List of Figures

Fig. 1. Schematic diagram of the experimental flare test facility showing the structure of the wake-stabilised jet flame in a cross-flow (not to scale).

Fig. 2. Spatial distribution of the grid quality metric M from temporal average LES solution for Case 1 ($R = 0.256$).

Fig. 3. Comparison of the mean mixture fraction obtained from temporal averaging over three successive intervals of 0.05s after 0.725s for Case 1 at $x/d = 2.0$.

Fig. 4. Predicted flame temperature contours: (a) instantaneous LES field, (b) time-averaged LES field, and (c) RANS averaged field. Flow conditions: u_j = 5.28 ms^{-1}, u_{cf} = 8.45 ms^{-1}, R = 0.256.

Fig. 5. Experimental photograph of natural gas flares: (a) short-time exposure (instantaneous) image, and (b) long-time exposure (averaged) image. Flow conditions: u_j = 2.09 ms^{-1}, u_{cf} = 4.09 ms^{-1}, R = 0.15 [2].

Fig. 6. Predicted flame temperature contours: (a) instantaneous LES field and (b) RANS field. Flow conditions: u_j = 5.28 ms^{-1}, u_{cf} = 0.45 ms^{-1}, R = 0.005.

Fig. 7. Predicted average U and V velocity profiles in the near-wake region (x/d = 2) at different vertical distances from the jet exit plane: (a, b) y/d = 2, (c, d) y/d = 0, and (e, f) y/d = -1.4 for Case 1.

Fig. 8. Predicted profiles of the x-y component of the Reynolds shear stress in the near-wake region (x/d= 2) at different vertical distances from the jet exit plane: (a) wake of the jet at y/d = 0, and (b) wake of the release pipe at y/d = -1.4 for Case 1.

Fig. 9. Predicted profiles of the turbulence intensity in the near-wake region (x/d = 2) at different vertical distances from the exit plane: (a) wake of the jet at y/d = 0, and (b) wake of the release pipe at y/d = -1.4 for Case 1.

Fig. 10. Predicted profiles of the turbulence intensity at different horizontal distances from the jet exit: (a) near field at x/d = 2.0, and (b) far field at x/d = 5.7 on the plane of symmetry.

Fig. 11. Predicted temperature contours on the y-z plane at different downstream distances from the jet exit, showing the gradual development of the counter-rotating vortex pair, from (a) LES and (b) RANS calculations. Flow conditions: u_j= 5.28 ms^{-1}, u_{cf} = 8.45 ms^{-1}, R = 0.256.

Fig. 12. Predicted temperature contours on the y-z plane at different downstream distances from the jet exit, showing the gradual development of the counter-rotating vortex pair, from (a) LES and (b) RANS calculations. Flow conditions: u_j= 0.46 ms^{-1}, u_{cf} = 5.2 ms^{-1}, R = 0.005.

Fig. 13. Predicted mean radial temperature profiles at two downstream distances from the jet exit: (a) x/d = 5.7 and (b) x/d = 22 for Case 1.

Fig. 14. Predicted RMS temperature fluctuations at two downstream distances from the jet exit: (a) x/d = 5.7 and (b) x/d = 22 for Case 1.

Tables

Table 1. Summary of the flow conditions simulated**.**

Case	u_j **(m s^{-1})**	u_{cf} **(m s^{-1})**	d_j **(cm)**	**Re$_w$**	**R**
1	5.28	8.45	5.25	28292	0.256
2	0.46	5.2	5.25	17410	0.005

Table 2. Comparison of the predicted species concentrations and flare combustion efficiency.

Parameters	**Experiment** %vol	**RANS** %vol	**LES** %vol
O_2	20.74	20.65	20.84
CO_2	0.103	0.085	0.12
$CO\times10^{-4}$	2.41	1.20	2.10
$CH_4\times10^{-4}$	4.80	2.50	6.00
$NO_x\times10^{-5}$	-	6.5	5.4
Efficiency (%)	99.21	99.51	99.33
Inefficiency (%)	0.79	0.49	0.67

Flow conditions: $u_j = 5.28$ ms^{-1}; $u_{cf} = 8.45$ ms^{-1}, $R = 0.256$

Figures

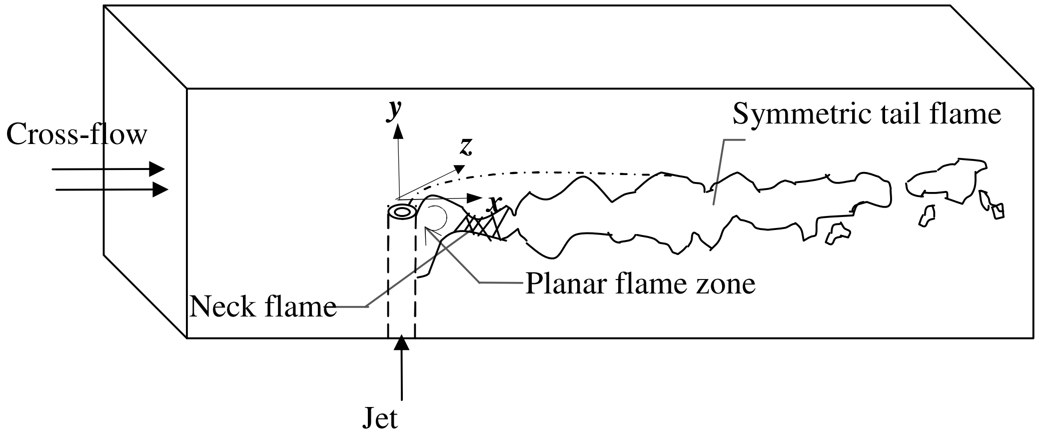

Fig. 1. Schematic diagram of the experimental flare test facility showing the structure of the wake-stabilised jet flame in a cross-flow (not to scale).

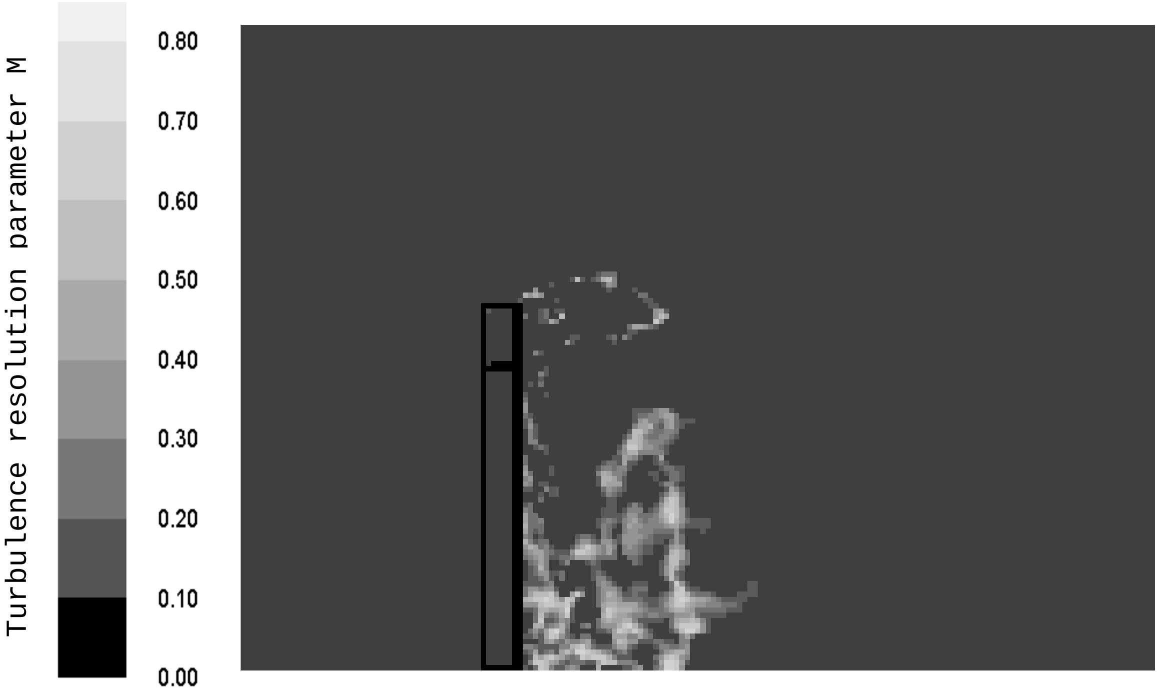

Fig. 2. Spatial distribution of the turbulence resolution parameter *M* on the mid-plane of the computational domain obtained from temporal average LES solution for Case 1 ($R = 0.256$).

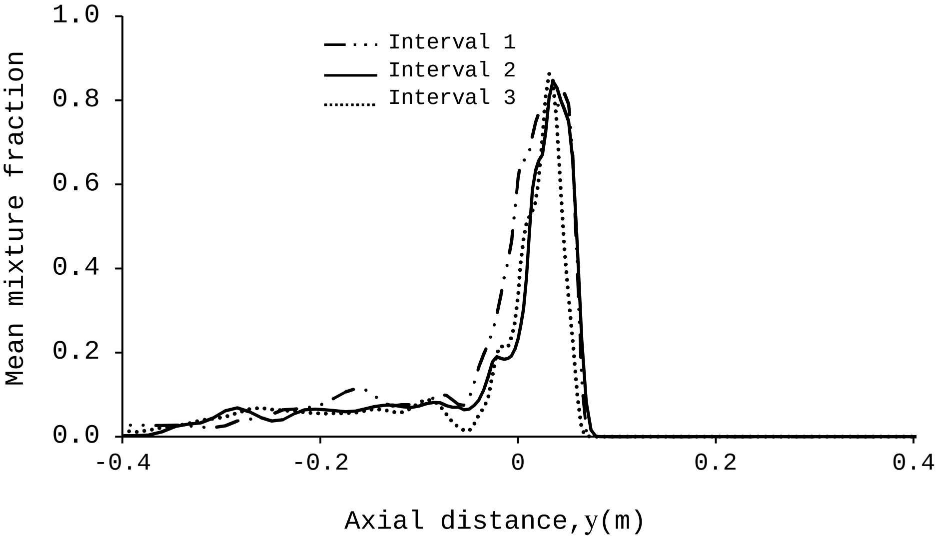

Fig. 3. Comparison of the mean mixture fraction obtained from temporal averaging over three successive intervals of 0.05s after 0.725s for Case 1 at *x/d* = 2.0.

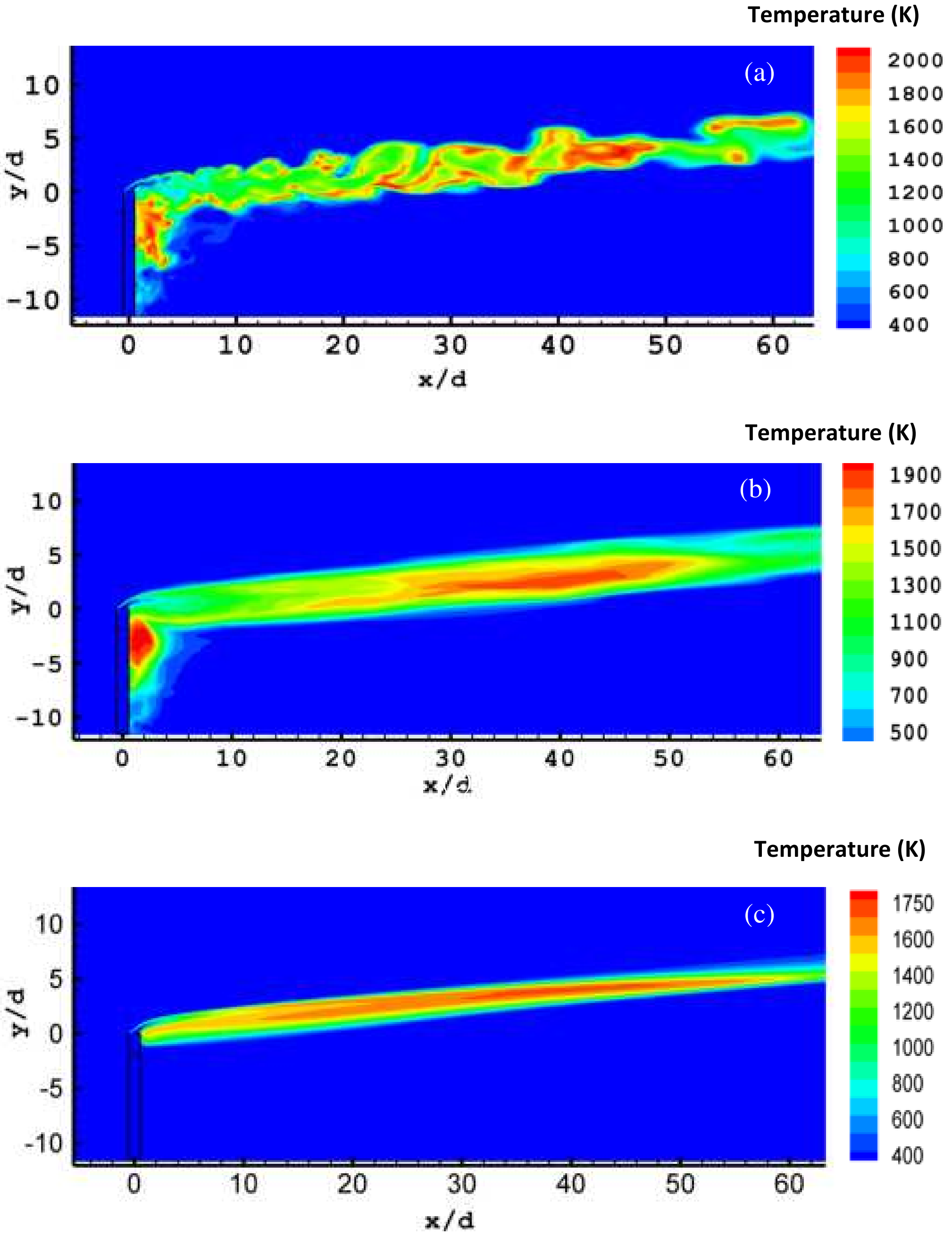

Fig. 4. Predicted flame temperature contours: (a) instantaneous LES field, (b) time-averaged LES field, and (c) RANS averaged field. Flow conditions: $u_j = 5.28$ ms^{-1}, $u_{cf} = 8.45$ ms^{-1}, $R = 0.256$.

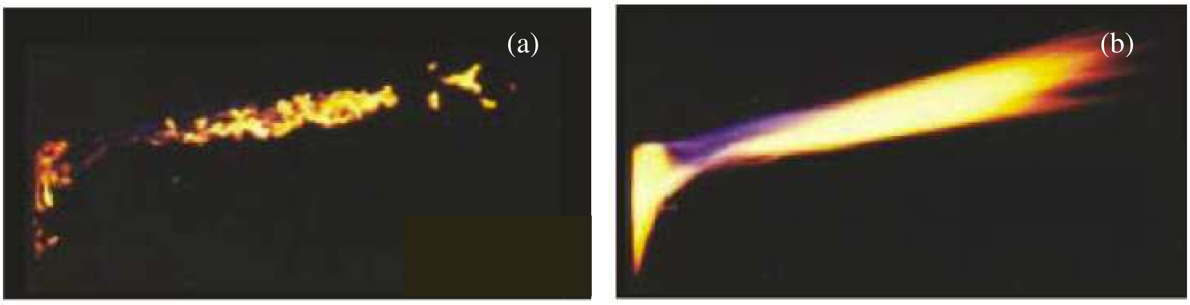

Fig. 5. Experimental photograph of natural gas flares: (a) short-time exposure (instantaneous) image, and (b) long-time (averaged) exposure image. Flow conditions: u_j = 2.09 ms^{-1}, u_{cf} = 4.09 ms^{-1}, R = 0.15 [2].

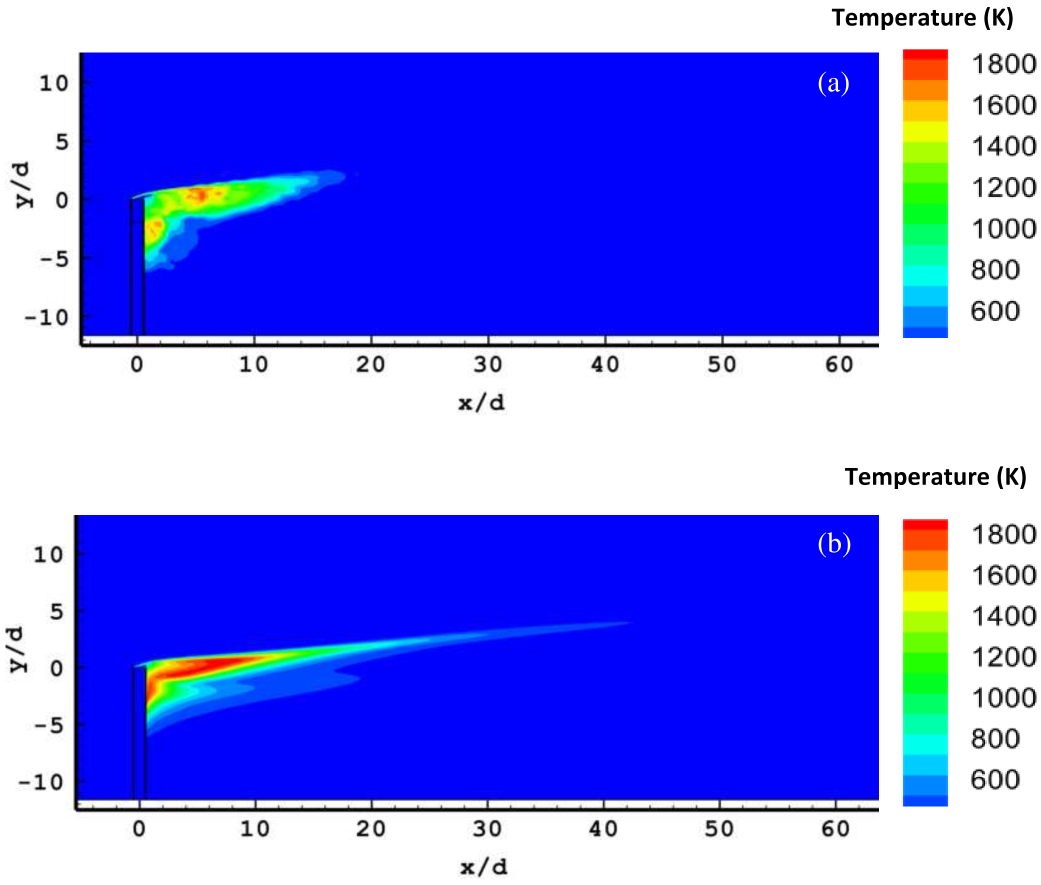

Fig. 6. Predicted flame temperature contours: (a) instantaneous LES field and (b) RANS field. Flow conditions: $u_j = 5.28$ ms^{-1}, $u_{cf} = 0.45$ ms^{-1}, $R = 0.005$.

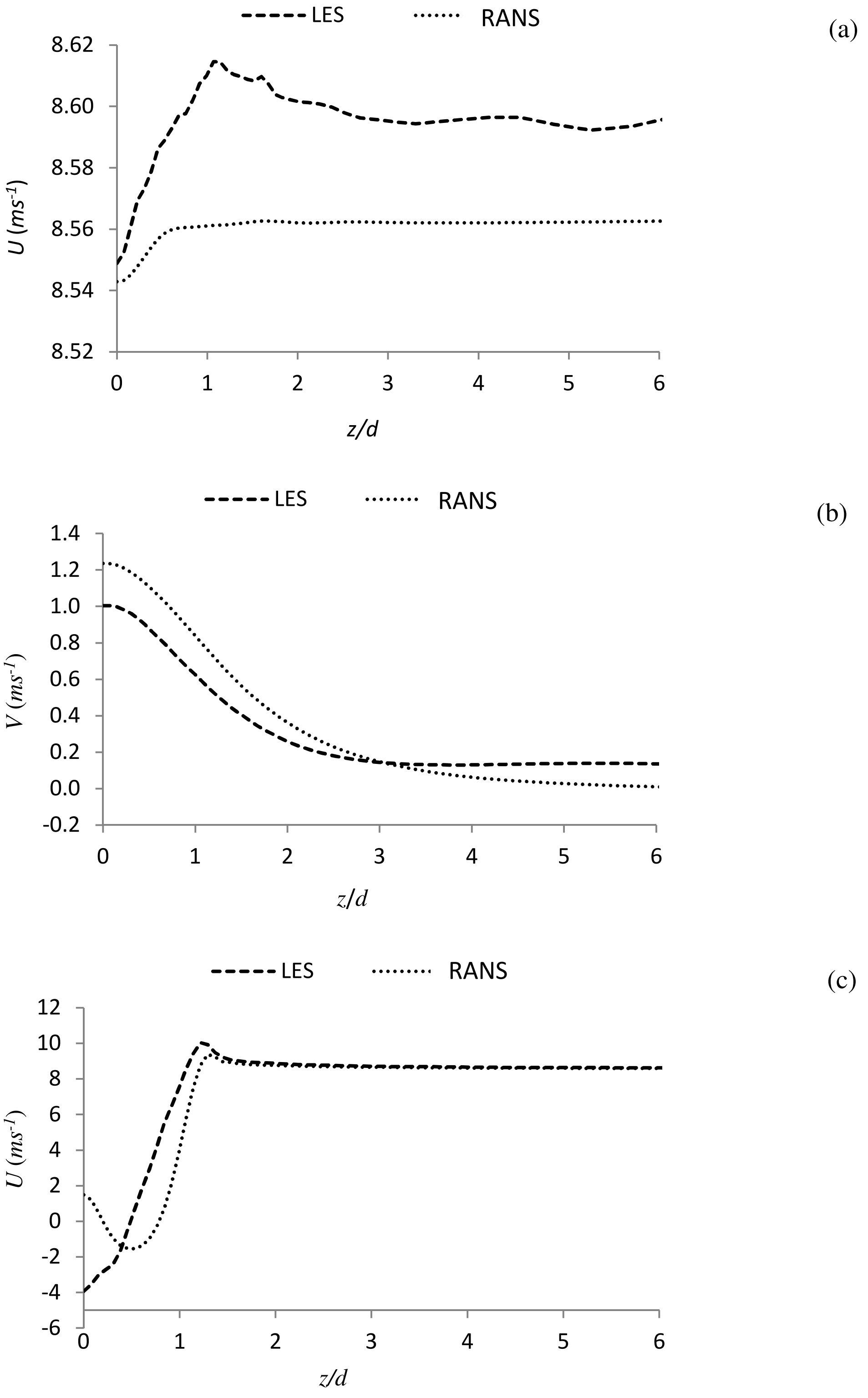

Fig. 7. Predicted average *U* and *V* velocity profiles in the near-wake region (x/d = 2) at different vertical distances from the jet exit plane: (a, b) y/d = 2, (c, d) y/d = 0, and (e, f) y/d = -1.4 for Case 1.

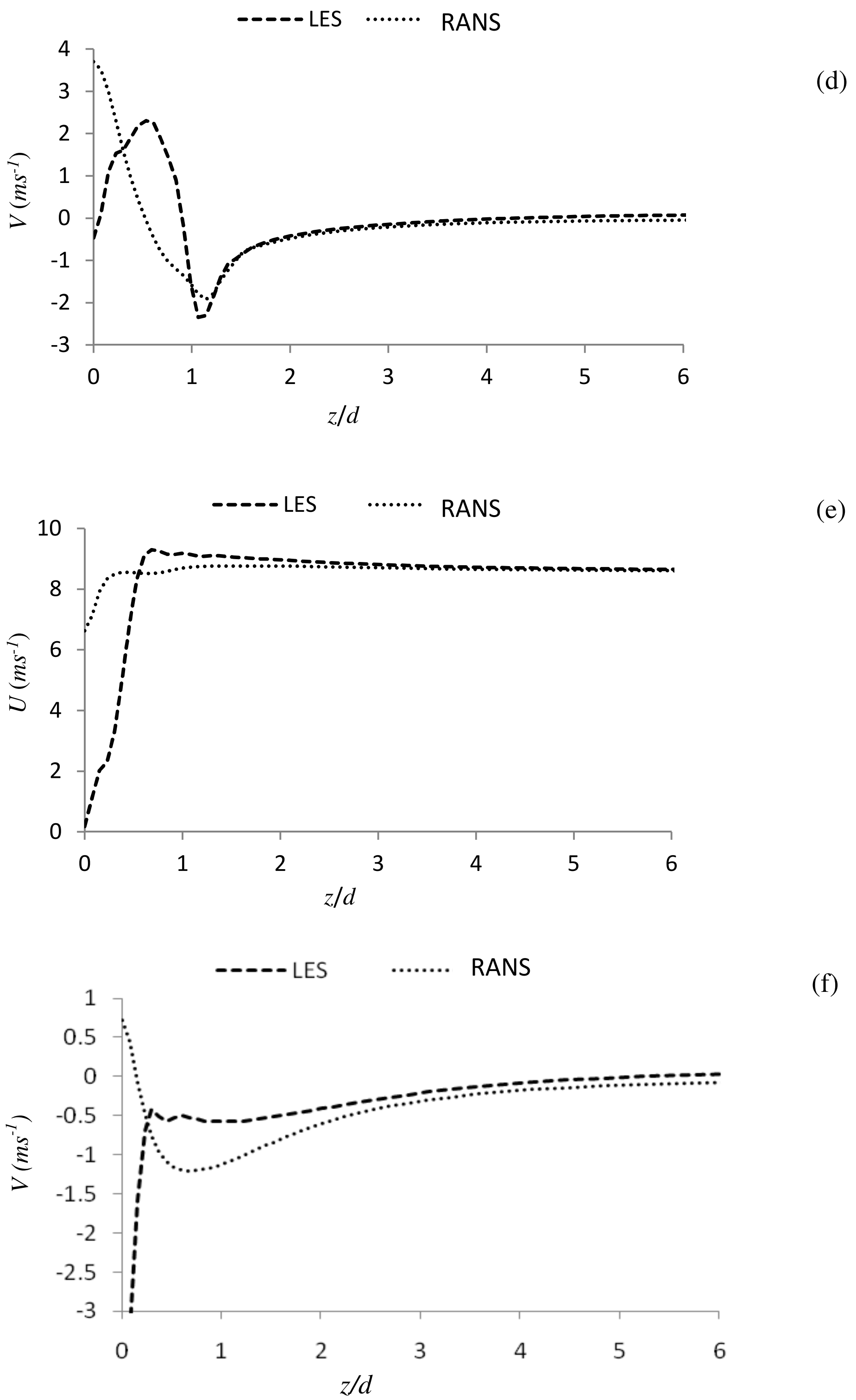

Fig. 7 (continued.) Predicted average *U* and *V* velocity profiles in the near-wake region (*x/d* = 2) at different vertical distances from the jet exit plane: (a, b) *y/d* = 2, (c, d) *y/d* = 0, and (e, f) *y/d* = -1.4 for Case 1.

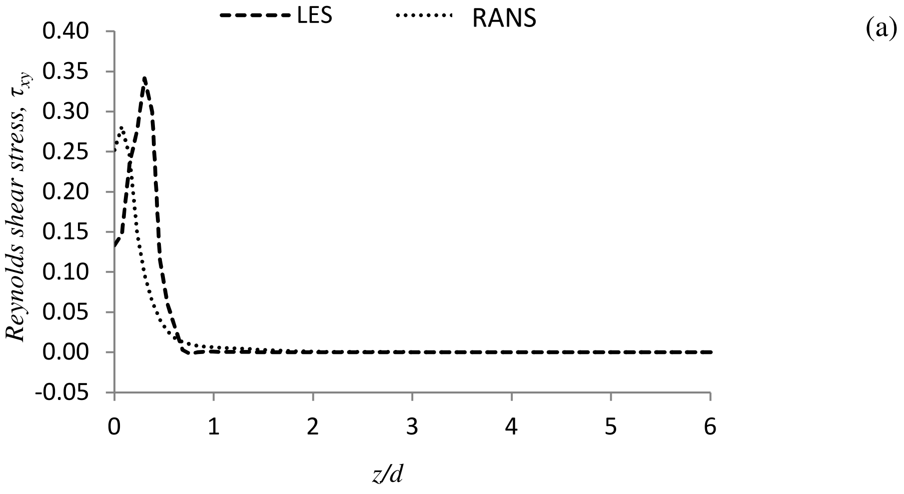

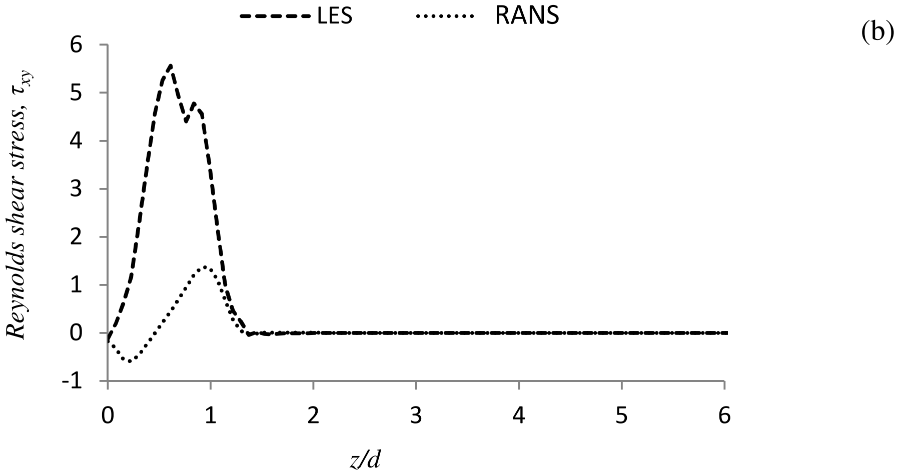

Fig. 8. Predicted profiles of the *x-y* component of the Reynolds shear stress in the near-wake region (*x/d*= 2) at different vertical distances from the jet exit plane: (a) wake of the jet at *y/d* = 0, and (b) wake of the release pipe at *y/d* = -1.4 for Case 1.

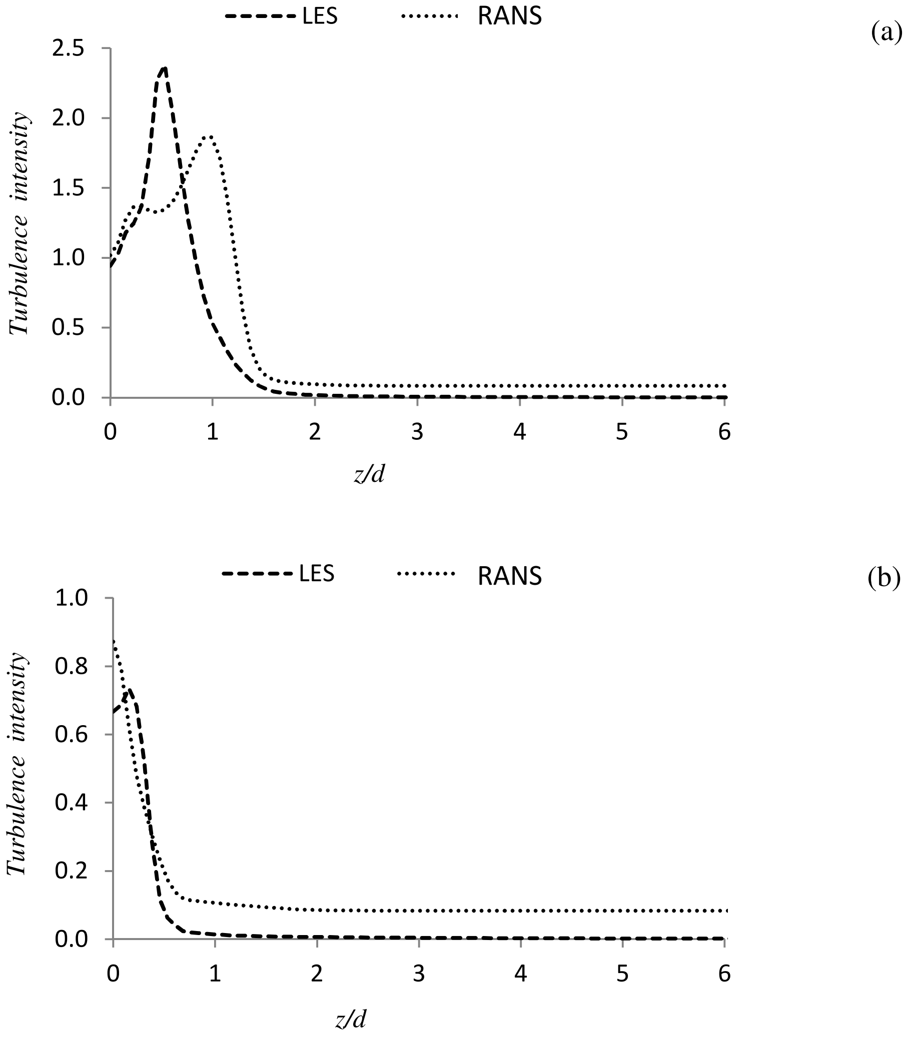

Fig. 9. Predicted profiles of the turbulence intensity in the near-wake region (*x/d* = 2) at different vertical distances from the exit plane: (a) wake of the jet at *y/d* = 0, and (b) wake of the release pipe at *y/d* = -1.4 for Case 1.

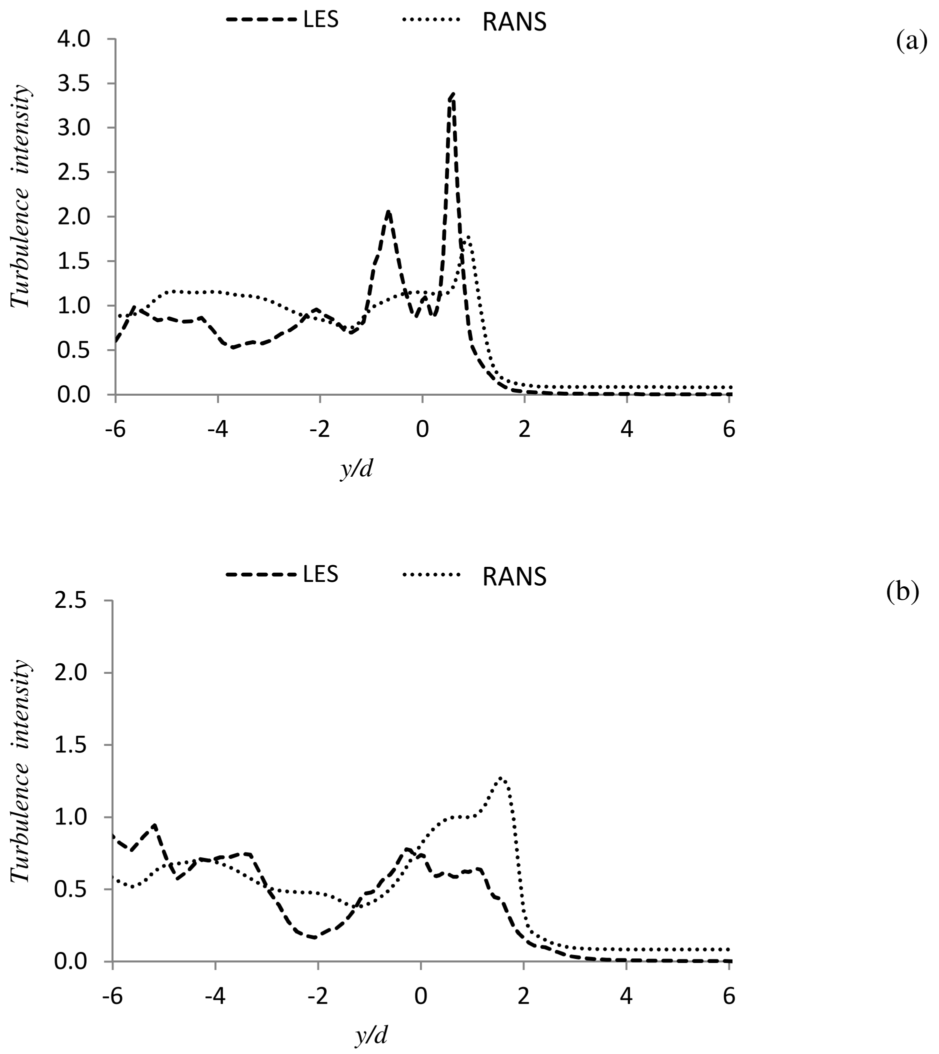

Fig. 10. Predicted profiles of the turbulence intensity at different horizontal distances from the jet exit: (a) near field at *x/d* = 2.0, and (b) far field at *x/d* = 5.7 on the plane of symmetry.

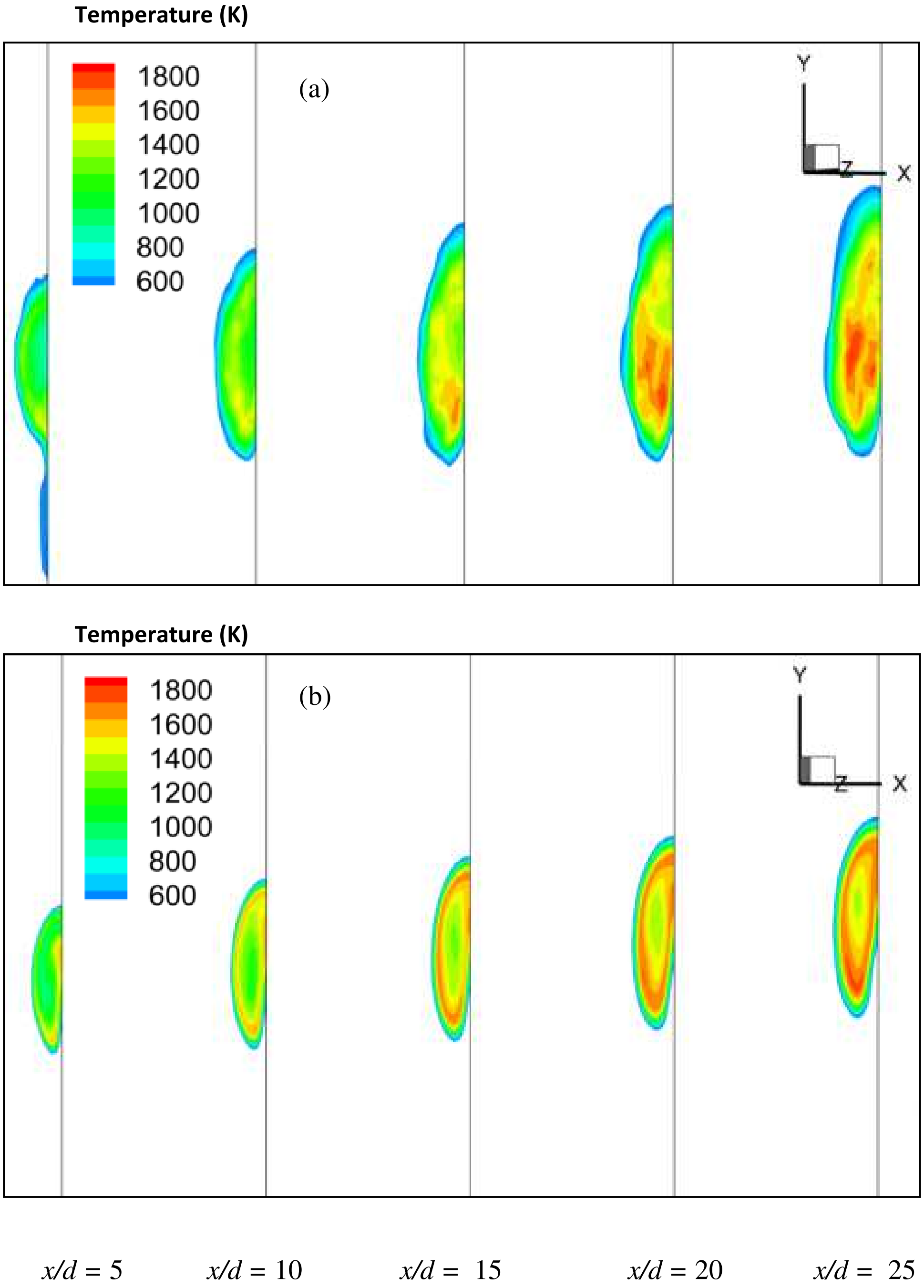

Fig. 11. Predicted temperature contours on the *y*-*z* plane at different downstream distances from the jet exit, showing the gradual development of the counter-rotating vortex pair, from (a) LES and (b) RANS calculations. Flow conditions: u_j= 5.28 ms^{-1}, u_{cf} = 8.45 ms^{-1}, R = 0.256.

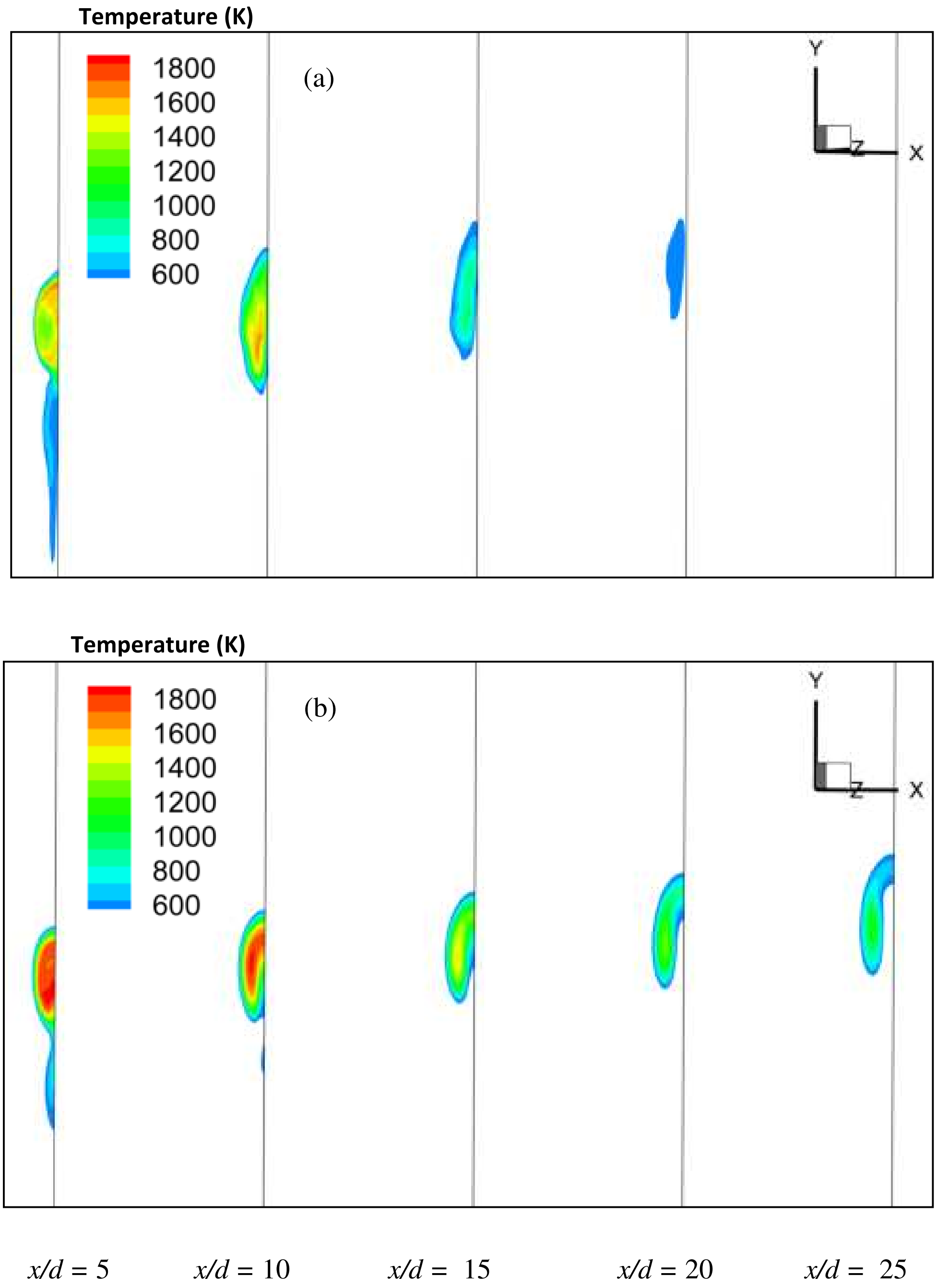

Fig. 12. Predicted temperature contours on the *y*-*z* plane at different downstream distances from the jet exit, showing the gradual development of the counter-rotating vortex pair, from (a) LES and (b) RANS calculations. Flow conditions: $u_j = 0.46$ ms^{-1}, $u_{cf} = 5.2$ ms^{-1}, $R = 0.005$.

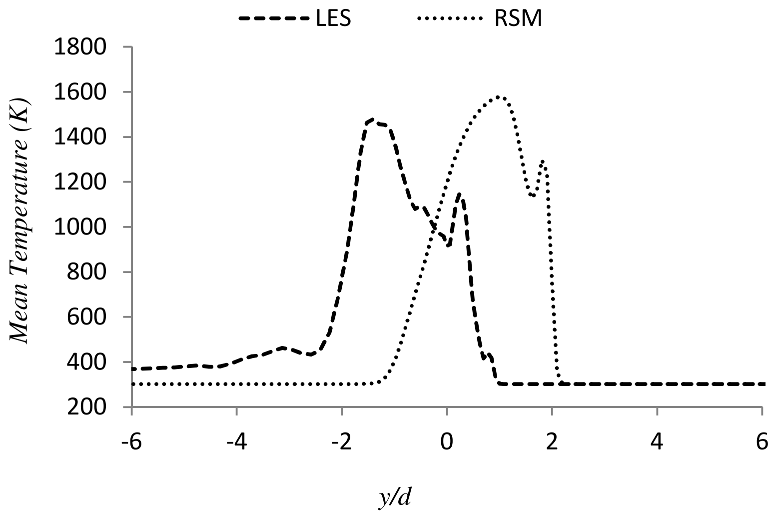

(a)

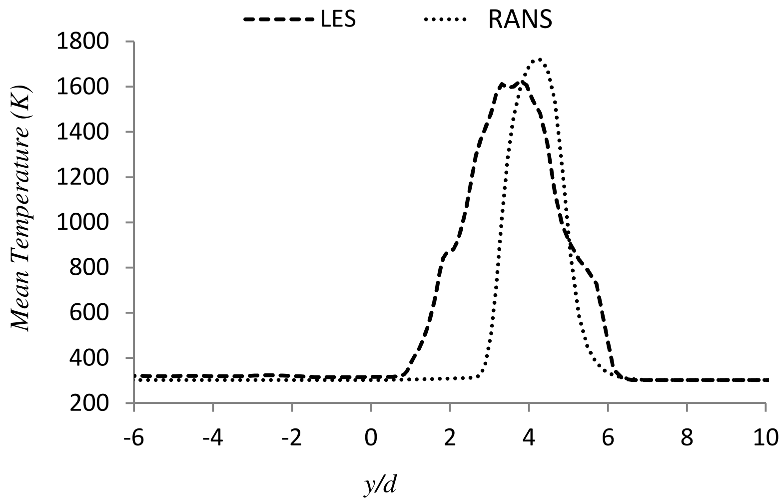

(b)

Fig. 13. Predicted mean radial temperature profiles at two downstream distances from the jet exit: (a) x/d = 5.7 and (b) x/d = 22 for Case 1.

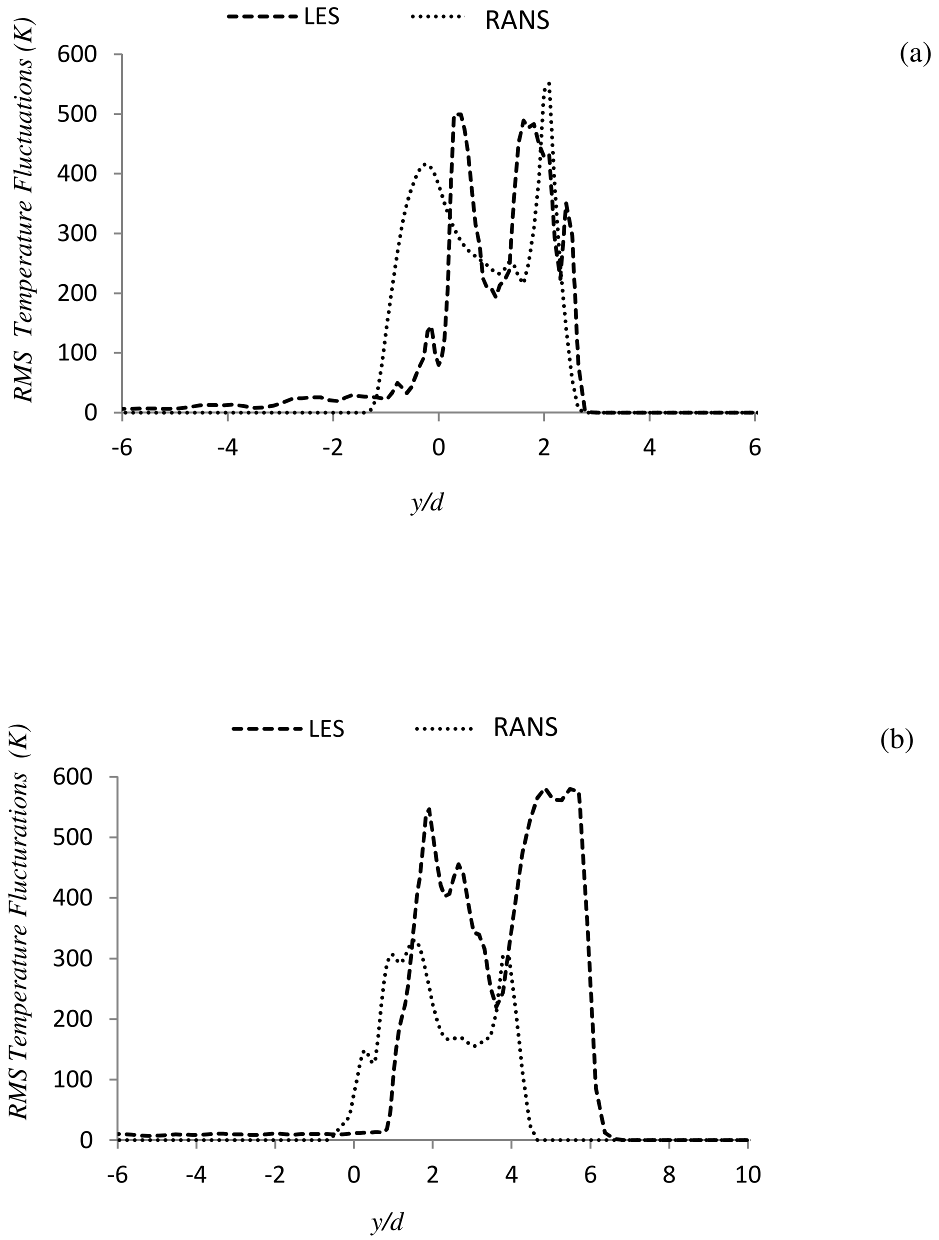

Fig. 14. Predicted RMS temperature fluctuations at two downstream distances from the jet exit: (a) *x/d* = 5.7 and (b) *x/d* = 22 for Case 1.